



## Efficient infrared light promoted degradation of volatile organic compounds over photo-thermal responsive Pt-rGO-TiO<sub>2</sub> composites

Juan-Juan Li<sup>a,b</sup>, Song-Cai Cai<sup>a,b,c</sup>, En-Qi Yu<sup>a,b,c</sup>, Bo Weng<sup>d,e</sup>, Xi Chen<sup>a,b,c</sup>, Jing Chen<sup>f</sup>,  
Hong-Peng Jia<sup>a,b,c,\*</sup>, Yi-Jun Xu<sup>d,e,\*\*</sup>



<sup>a</sup> CAS Center for Excellence in Regional Atmospheric Environment, Institute of Urban Environment, Chinese Academy of Sciences, Xiamen, 361021, PR China

<sup>b</sup> Key Laboratory of Urban Pollutant Conversion, Institute of Urban Environment, Chinese Academy of Sciences, Xiamen, 361021, PR China

<sup>c</sup> University of Chinese Academy of Sciences, Beijing, 100049, PR China

<sup>d</sup> State Key Laboratory of Photocatalysis on Energy and Environment, College of Chemistry, New Campus, Fuzhou University, Fuzhou, 350116, PR China

<sup>e</sup> College of Chemistry, New Campus, Fuzhou University, Fuzhou, 350116, PR China

<sup>f</sup> Xiamen Institute of Rare-earth Materials, Haixi Institutes, Chinese Academy of Sciences, Xiamen, Fujian, 361021, PR China

### ARTICLE INFO

#### Keywords:

Pt-rGO-TiO<sub>2</sub>

IR light

Photo-thermocatalysis

VOCs

### ABSTRACT

Infrared (IR) light photo-thermocatalysis has been motivated by the realization of prospects that sunlight is an inexhaustible energy source where infrared photons most strongly emitted in the solar spectrum are converted into thermal energy, which thus can drive different redox catalysis applications, e.g., oxidative degradation of volatile organic compounds (VOCs). Herein, we report that the hybrid nanomaterial Pt-rGO-TiO<sub>2</sub>, featuring the broad light wavelength absorption (800–2500 nm), can be used as a highly active photo-thermal responsive catalyst for efficient VOCs decomposition under IR irradiation. The maximum photo-thermal conversion efficiency is able to reach 14.1% with a significant toluene conversion of 95% and CO<sub>2</sub> yield of 72% under infrared irradiation intensity of 116 mW/cm<sup>2</sup>, along with retaining its stability for nearly 50 h. The comparison characterizations evidence that such excellent performance is predominantly attributed to the synergistic effects of efficient light-to-heat conversion, increased adsorption capacity and well dispersed supported Pt-TiO<sub>2</sub> catalyst on the 2D rGO sheet. This work highlights that graphene-based composites as IR light photon absorber show great promise for redox reactions through photo-thermal effect, which provides an alternative and feasible strategy for solar energy conversion.

### 1. Introduction

Volatile organic compounds (VOCs) emitted into the atmosphere from anthropogenic have led to photochemical smog and ground-level ozone [1]. The commercial heterogeneous catalytic reactions with oxides of transition metal are driven by thermal energy for complete oxidation of VOCs [2], but high operating temperatures involved in this process generally require external electrical heating and are characterized by low energy efficiencies and compromised durability of catalysts [3]. Since solar power is an inexhaustible energy source [4], researchers have long been infatuated with the idea of converting light into chemical energy via photocatalysis to generate highly reactive oxidative species (ROSSs, e.g., holes or superoxide/hydroxyl radicals) to address air pollution problems [5]. For the most extensively studied semiconductor TiO<sub>2</sub> photocatalyst, the limited light absorption (only UV, 3% of solar light), high charge carriers recombination and lack of

highly active sites on catalyst surface render such photochemical conversion inefficient [6]. Sunlight consists of about 44% visible light, and therefore multifarious strategies [7–9] such as doping with metals and/or nonmetals, adopting organic sensitizers or coupling with other semiconductors, were developed in an attempt to extend the photo-response toward improving the efficiency of TiO<sub>2</sub>. However, many developed TiO<sub>2</sub>-based or non-TiO<sub>2</sub>-based photocatalysts [10,11] cannot be activated by the IR wavelength light that constitutes 53% of the solar energy reaching earth's surface [12].

In order to effectively utilize IR light, tremendous attempts have been made to develop IR-light-induced photocatalysts. Owing to the low photon energy and unsuitable band structure, small bandgap semiconductors with protruding NIR light adsorption, were generally deemed to lack photocatalytic activity [13]. Thus, many works have focused mainly on upconversion luminescence of rare-earth materials [14–17] through converting near infrared (NIR) excitation into UV or

\* Corresponding author at: CAS Center for Excellence in Regional Atmospheric Environment, Institute of Urban Environment, Chinese Academy of Sciences, Xiamen, 361021, PR China.

\*\* Corresponding author at: State Key Laboratory of Photocatalysis on Energy and Environment, College of Chemistry, New Campus, Fuzhou University, Fuzhou, 350116, PR China.

E-mail addresses: [hpjia@iue.ac.cn](mailto:hpjia@iue.ac.cn) (H.-P. Jia), [yjxu@fzu.edu.cn](mailto:yjxu@fzu.edu.cn) (Y.-J. Xu).

visible emission to trigger photocatalytic reaction. For instance, by assembling  $\text{NaYF}_4\text{-Yb/Tm}$ @ $\text{NaYF}_4$  up-converting core-shell nanoparticles (NPs) with UV active  $\text{ZnO}$  NPs [18], organic molecules were photocatalytically degraded under NIR light. Although this work manifested the possibility of using NIR light for photocatalysis, the efficiency of NIR light energy transfer upconversion process was largely limited by its very narrow absorption band of light at 980 nm and the quick depletion of excitation energy [19,20]. In contrast to traditional rare-earth up-converting materials, carbon quantum dots (CQDs) are not limited to specific wavelength of light, and recent improvement has been made in using CQDs as up-conversion material in combination with developed UV- or visible-light-active NPs (i.e., CQDs/ $\text{Cu}_2\text{O}$  composites [21], CQDs/H-TiO<sub>2</sub> nanobelt [22]) as NIR-responsive photocatalyst. Unfortunately, up-conversion efficiency of CQD was primarily restricted by the competition between up-conversion and down-conversion processes. Moreover, sparked by the discovery that the rare-earth cations are able to absorb IR light [23],  $\text{BiErWO}_6$  solid solution [24], a regular stacking of  $\text{BiErO}_2$  layers interleaved with  $\text{WO}_4$  layers, was successfully constructed as an efficient NIR photocatalyst for the degradation of rhodamine B. Additionally, microcrystal of  $\text{Cu}_2(\text{OH})\text{PO}_4$  [25] was found to be a NIR-activated photocatalyst in which the hot electrons are generated at the  $\text{CuO}_4(\text{OH})$  trigonal bipyramids and transfer to the neighboring  $\text{CuO}_4(\text{OH})_2$  octahedra for efficient electron-hole separation. Recently, Localized surface plasmon resonances (LSPR) also offer an exciting opportunity to design artificial materials with effective IR light harvesting for plasmonic photocatalysis applications [26–29]. For instance,  $\text{Cu}_7\text{S}_4$  NPs utilized NIR photon through LSPR in which hot holes could be generated from the photoexcitation of  $\text{Cu}_7\text{S}_4$  NPs under IR light illumination and quickly injected into Pd domain to render hole-rich Pd surface for photocatalytic oxidation of benzyl alcohol and for hydrogenation of nitrobenzene [30].

Despite the recent progress in searching strategies for effective exploitation of IR light, the IR-light-induced photocatalysis efficiency is still not satisfactory to date due to the limited utilization of photo-generated charge carriers, which impedes its practical application. In contrast, the strong thermal effect induced by IR photon energy, especially on the IR-induced photo-thermocatalysis for environmental pollutants purification, has been significantly overlooked. Drawing inspiration from near-IR light photosensitizers largely exploited in photo-thermal cancer therapy [31–33], there has been a resurgence of research interest in an exploration of IR photo-thermal responsive materials. For example, Hu and co-workers recently have reported that photo-thermal effect is utilized in core-shell  $\text{Fe}_3\text{O}_4@\text{SiO}_2$  to capture the energy of IR light for photo-thermal catalytic oxidation of NO [34]. Therefore, IR-driven photo-thermocatalysis provides an alternative approach to solar energy utilization and opens the possibility of substituting light-driven photo-thermocatalysis reactions for conventional thermal-based catalytic redox reactions.

In principle, to achieve high photo-thermal energy conversion efficiency, an ideal material must satisfy several functional requirements: robust harvesting of IR light, forceful coupling of the harvested photons into thermal energy and effective catalytic active sites. Graphene, a single-layer carbon sheet with a hexagonal packed lattice structure, has inspired tremendous interest due to its unique physic-chemical properties such as high thermal conductivity, excellent carriers mobility, and good optical transparency [35,36]. So far, the main focus of interest has been on electronic properties, i.e., photoelectron mediator and acceptor in graphene-based composite photocatalysts. Due to its high optical absorption in the NIR region, a new direction for graphene-based composites is photo-thermal effect [37], and one remarkable application is its potential use in photo-thermal therapy for the ablation of cancerous cells whereby NIR light is absorbed and converted into heat [38,39]. In addition, the photo-thermal effect of reduced graphene oxide (rGO) sheets can make the electrons obtain more energy and move faster on the hot rGO sheet to promote the degradation of methyl blue over the rGO-P25 composites [40].

With these motivations, we report that the photo-thermal responsive hybrid nanomaterial of Pt-rGO-TiO<sub>2</sub> can be used for efficient degradation of VOCs under IR light. The results showed that photo-thermal responsive 1% Pt-rGO-TiO<sub>2</sub> composites exhibited high catalytic performance with 95% of toluene conversion, 72% of CO<sub>2</sub> yield and long term stability of nearly 50 h toward degradation of VOCs under IR light. The comparative characterizations revealed that such photo-thermal catalytic activity enhancement results from the restacking-inhibited 2D rGO sheet, by which the synergistic effects of efficient light-to-heat conversion, increased adsorption capacity and supported active Pt NPs can be achieved. This work highlights that graphene-based composites, featuring the broad IR light absorption, show promise for redox catalysis applications through photo-thermal effect, which would open a new promising route to using graphene-based composite materials as IR light photon absorber for solar energy conversion.

## 2. Experimental section

### 2.1. Preparation of graphene oxide

Graphene oxide (GO) was synthesized from natural graphite powder by a modified Hummers method [37,41]. In detail, 2 g of graphite powder (Alfa Aesar) was put into a mixture of 50 mL of concentrated H<sub>2</sub>SO<sub>4</sub> and 1 g of NaNO<sub>3</sub> in an ice water bath and 8 g of KMnO<sub>4</sub> was added gradually for 120 min under vigorous stirring. Then, the solution was heated to 35 °C in an oil-bath and kept stirring for 2 h. Successively, 50 mL of deionized (DI) water was added into the above mixture, followed by stirring at 95 °C for 0.5 h. Then, to the resulting mixture were added 50 mL of DI water and 20 mL of 30% H<sub>2</sub>O<sub>2</sub> to remove unreacted KMnO<sub>4</sub>. When cooled to room temperature, the supernatant then underwent two more high-speed centrifugation steps at 8000 rpm for 10 min, then washed with 5% HCl aqueous solution to remove metal ions followed by DI water to remove the acid. The product was ultrasonicated for 1.5 h, then stirred under ambient condition overnight. The mixture was then carefully diluted with deionized (DI) water, filtered, and washed until the pH of rinse water became neutral. Finally, a homogeneous GO aqueous solution (4 mg/mL) was obtained.

### 2.2. Preparation of Pt-rGO-TiO<sub>2</sub> composites

To synthesize the Pt-reduced graphene oxide-TiO<sub>2</sub> (x% Pt-rGO-TiO<sub>2</sub>) composites with various ratios of Pt, a simple solvothermal method using ethanol-water as solvent was used as the following [42], where titanium dioxide (TiO<sub>2</sub>) nanopowder is the commercial P25 (Degussa). 7.5 mL of GO aqueous solution (4 mg/mL) was ultrasonicated in a 15 mL of deionized water and 11.25 mL of anhydrous ethanol solution to disperse it well; after that, 0.6 g of TiO<sub>2</sub> first, then certain amount of H<sub>2</sub>PtCl<sub>6</sub> (3.8 mg/mL) aqueous solution was then rapidly injected into the above GO solution by pipet to prepare 0.1, 0.5, 1 and 2 wt% Pt-rGO-TiO<sub>2</sub> nanocomposite catalysts. The mixing solution was aged with vigorous stirring for 2 h to obtain a homogeneous suspension. Then, this suspension was transferred to a 50 mL teflon-sealed autoclave and maintained at 120 °C for 24 h. Under such a solvothermal condition, the solvent of ethanol-water has the strong power to simultaneously reduce Pt<sup>4+</sup> and GO into Pt and rGO [43]. The resulting composites were filtered and washed with deionized water, and fully dried at 60 °C in vacuum oven to get the final x% Pt-rGO-TiO<sub>2</sub> composites.

For comparison, the preparation procedure of TiO<sub>2</sub>, rGO-TiO<sub>2</sub> and 1% Pt-TiO<sub>2</sub> was similar to that of x% Pt-rGO-TiO<sub>2</sub> without addition of rGO and/or Pt solution.

### 2.3. Catalyst characterization

Powder X-ray diffraction (XRD) characterization was carried out on a X'Pert Pro automatic powder diffractometer operated at 40 kV and

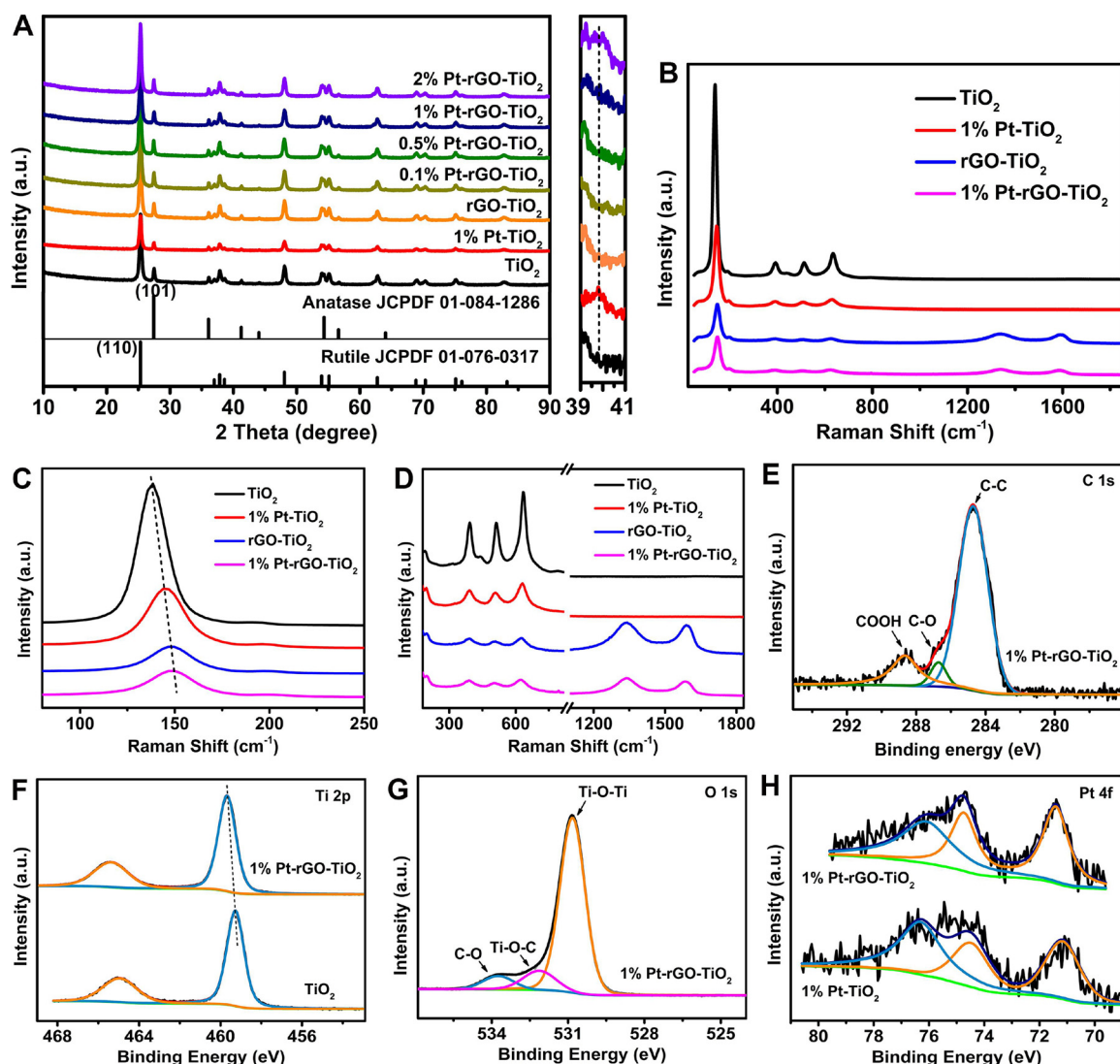


Fig. 1. XRD patterns (A); Raman spectra (B) and the enlarged view in (C) and (D); XPS spectra of the C 1s (E), Ti 2p (F), O 1s (G), and Pt 4f (H) of the samples.

40 mA using  $\text{Cu K}\alpha$  monochromatized radiation. Raman spectroscopy was carried out on LabRAM Aramis using a green laser of 532 nm wavelength. The actual loading content of noble metal was determined by inductively coupled plasma atomic emission spectroscopy (ICP-AES, Varian, VISTAMPX-ICP). Nitrogen adsorption-desorption measurements of the catalysts were performed on a Quantachrome autosorb iQ2 adsorption automatic instrument at liquid nitrogen temperature. All samples were degassed under vacuum at 60 °C for 24 h before the measurement. The specific surface area and pore volume of the catalysts were calculated from the nitrogen adsorption-desorption isotherms using the Brunauer-Emmett-Teller (BET) and Barrett-Joyner-Halenda (BJH) methods. Diffuse reflectance spectra were recorded using a Varian Cary 5000 UV-vis spectrophotometer in the 200–2500 nm range at room temperature using  $\text{BaSO}_4$  as a reference. XPS analysis was conducted on a Thermo Scientific ESCALAB 250 with a monochromatized microfocused Al X-ray source. Transmission electron microscopy (TEM) was analyzed using a JEOL model JEM 2100 EX instrument at an acceleration voltage of 200 kV. Temperature-programmed desorption (TPD) measurement was performed on a Quantachrome Chemstar instrument. 200 mg catalyst sample was filled in an adsorption vessel and pretreated in a He flow (50 ml/min) at 300 °C for 60 min then cooled to 35 °C and kept at this temperature for 60 min in a flow of 5 vol%  $\text{O}_2/\text{He}$  or gaseous toluene (30 ml/min). Then, the sample was swept with He for 120 min and heated to 800 °C

at a rate of 10 °C/min in a He flow of 30 ml/min. The desorbed products were monitored simultaneously by thermal conductivity detector and mass spectroscopy equipment. The enthalpy of samples was obtained by using differential scanning calorimeter (Netzsch STA 449 F3, Thermal Analysis Corporation, Germany) from 30 to 300 °C at a heating rate of 5 °C/min in a  $\text{N}_2$  flow of 50 ml/min. Electron paramagnetic resonance (EPR) spectra were taken from Bruker A300 spectrometer by applying an X-band (9.43 GHz, 1.5 mW) microwave and sweeping magnetic field at room temperature. *In situ* DRIFTS was performed on a FTIR spectrometer (Nicolet Nexus 670) equipped with a smart collector and a MCT/A detector. Prior to experiment, the sample was pretreated at 150 °C for 1.5 h in a  $\text{N}_2$  flow to remove adsorbed impurities. The background spectrum was collected under  $\text{N}_2$  and automatically deducted from the sample spectra. Afterward, 1000 ppm toluene/ $\text{N}_2$  was introduced to the cell at a flow rate of 50 mL/min at 150 °C, and then DRIFTS spectra were recorded. Subsequently, the flow of  $\text{N}_2$  was introduced to investigate the reactivity at 150 °C.

#### 2.4. Photo-thermocatalytic activity

The photo-thermocatalytic activity of the samples for toluene oxidation was evaluated in a cylindrical stainless steel reactor with a quartz window under IR light irradiation (375 W, Philips) with a 800 nm cut-off filter. In the experiments, an ethanol suspension

containing 0.1 g of the catalyst was prepared, and then coated on a fiberglass membrane of 50 mm diameter, dried at 40 °C and finally placed on the photoreactor. Prior to irradiation, the adsorption-desorption equilibrium of toluene on the photocatalyst was carried out. The equilibrium concentration of toluene was about 200 ppm produced by an air stream bubbling through a liquid toluene. The flow rate of the gas was 52.2 mL min<sup>-1</sup>. The concentration of toluene and the evolution of CO<sub>2</sub> were monitored by an on-line gas chromatograph equipped with two flame ionization detectors (FID) and a nickel-based methanizer. The toluene conversion and CO<sub>2</sub> yield for the photocatalytic reaction were calculated by using Eqs. (1) and (2), respectively.

$$\text{Toluene conversion (\%)} = 100 \times ([\text{Toluene}]_{\text{in}} - [\text{Toluene}]_{\text{out}})/[\text{Toluene}]_{\text{in}} \quad (1)$$

$$\text{CO}_2 \text{ yield (\%)} = 100 \times [\text{CO}_2]_{\text{produced}}/[\text{CO}_2]_{\text{theoretical}} \quad (2)$$

## 2.5. Photocatalytic activity

The photocatalytic activity of the catalyst for toluene oxidation was measured in a cylindrical quartz reactor (5 cm × 5 cm × 1 cm) with a glycerol-water bath of ultralow temperature (−20 °C) to keep the reaction temperature at room temperature (28 °C) under the irradiation of IR lamp.

## 2.6. Thermocatalytic activity

The thermocatalytic activity of the catalyst for toluene oxidation was carried out in a cylindrical stainless steel reactor on an online gas-phase reaction apparatus at different temperature by external electrical heating.

## 3. Results and discussion

Fig. 1(A) displays the XRD patterns of the bare TiO<sub>2</sub>, rGO-TiO<sub>2</sub> and Pt-rGO-TiO<sub>2</sub> composites with various loading amounts of Pt NPs. All of identified peaks of the samples are perfectly in accordance with anatase TiO<sub>2</sub> (JCPDS card no. 01-084-1286) and rutile TiO<sub>2</sub> (JCPDS card no. 01-089-0554). Moreover, no typical diffraction peaks assigned to Pt NPs have been observed in x% Pt-rGO-TiO<sub>2</sub> composites (x = 0, 0.1, 0.5 and 1), which could be ascribed to the low content of small sized Pt [44], whereas a small peak at 41° for Pt NPs was observed in 1% Pt-TiO<sub>2</sub> and 2% Pt-rGO-TiO<sub>2</sub> samples, which might be attributed to high loading or Pt with large particle size. Likewise, no diffraction peaks for rGO were detected in rGO-TiO<sub>2</sub> and x% Pt-rGO-TiO<sub>2</sub> composites due to the small amount and weak intensity of rGO which might be shielded by the peak of TiO<sub>2</sub> at 25.3° [45]. Raman spectroscopy has been applied to further distinguish the sp<sup>2</sup> and sp<sup>3</sup> hybridization in the carbon-based materials [46]. As shown in Fig. 1(B), the bare TiO<sub>2</sub> exhibits five intensive peaks of anatase TiO<sub>2</sub>(A) where the peaks at 144, 196 and 636 cm<sup>-1</sup> are assigned to the E<sub>g</sub> mode of TiO<sub>2</sub>(A), and the peaks at 396 cm<sup>-1</sup> and 517 cm<sup>-1</sup> correspond to the B<sub>1g</sub> mode of TiO<sub>2</sub>(A) and doublet of A<sub>1g</sub>/B<sub>1g</sub> [47]. No obvious peaks corresponding to rutile TiO<sub>2</sub>(R) are observed, presumably since the peaks are too weak to be clearly observed. These peaks are also observed in 1% Pt-TiO<sub>2</sub>, rGO-TiO<sub>2</sub>, 1% Pt-rGO-TiO<sub>2</sub> composites, but their intensities decrease significantly, and even shift to a high wavenumber (Fig. 1(C) and (D)), thereby indicating that the symmetric stretching vibration of O-Ti-O in TiO<sub>2</sub> has been destroyed to some extent after combination with Pt or/and rGO [48]. The peak shift can be attributed to a change of surface strain stemming from the introduction of Pt or/and rGO which shows a strong interaction with oxygen in TiO<sub>2</sub> [49]. For the rGO-TiO<sub>2</sub> and 1% Pt-rGO-TiO<sub>2</sub> composites, two typical features (D and G bands) of rGO at 1335 cm<sup>-1</sup> and 1591 cm<sup>-1</sup> (Fig. 1 (D)), respectively, are observed, where the D band corresponds to ring breathing modes of sp<sup>2</sup> carbon atoms adjacent to a defect or an edge and the G band is associated with sp<sup>2</sup> carbon atoms in

a planar and conjugated structure [50].

X-ray photoelectron spectroscopy (XPS) was employed to inspect the interactions among Pt, TiO<sub>2</sub> and rGO as well as the chemical states of elements. The peak deconvolutions of C 1s, Ti 2p, O 1s and Pt 4f are shown in Fig. 1(E)–(H). The deconvoluted C1s peaks located at 284.7, 286.7 and 288.6 eV are characteristic of C–C, C–O and COOH, respectively, indicating a significant deoxygenation of oxygen-containing functional groups of GO and effective reduction of GO to rGO [51,52]. The two deconvoluted Ti 2p peaks centered at 459.7 and 465.4 eV are assigned to the core levels of Ti<sup>4+</sup> 2p<sub>3/2</sub> and Ti<sup>4+</sup> 2p<sub>1/2</sub> [53], which are slightly shifted toward a higher binding energy compared with those in TiO<sub>2</sub>, revealing the change in the chemical environment of Ti in 1% Pt-rGO-TiO<sub>2</sub> composites due to the formation of Ti–O–C bond [45], since oxygen is highly electronegative and it removes the electron density from the Ti of the 1% Pt-rGO-TiO<sub>2</sub> composites [53]. The three deconvoluted O 1s bands located at 530.8, 532.1 and 533.8 eV correspond to Ti–O–Ti (lattice O), Ti–O–C and C–O groups, respectively [45], where the existence of the Ti–O–C bond demonstrates that rGO is intensively attracted to TiO<sub>2</sub>. The characteristic peaks of Pt 4f<sub>5/2</sub> and Pt 4f<sub>7/2</sub> located at 71.4 eV and 74.7 eV are assigned to the core levels of Pt° [54]. The XPS results further convince the incorporation of Pt and rGO into TiO<sub>2</sub>, and the presence of the interaction between the Pt/rGO and TiO<sub>2</sub>, which is consistent with the Raman analysis.

UV-vis diffuse reflectance spectra (DRS) measurement was performed to evaluate the optical response of the catalysts. Fig. 2 plots the absorption spectra of the x% Pt-rGO-TiO<sub>2</sub> (x = 0, 0.1, 0.5, 1 and 2) composites as compared with those of bare TiO<sub>2</sub> and 1% Pt-TiO<sub>2</sub>. The bare TiO<sub>2</sub> looks pale white (inset in Fig. 2) and displays a typical absorption with an intense transition in the UV region, as a result of the electron transitions from the valence band to the conduction band (O<sub>2p</sub> → Ti<sub>3d</sub>) in the intrinsic band gap absorption of TiO<sub>2</sub> [55], but with almost no absorption in the Vis-IR. Compared with TiO<sub>2</sub>, all Pt-rGO-TiO<sub>2</sub> composites exhibit an enhanced absorption in the Vis-IR region with no obvious red shift at the absorption. For the TiO<sub>2</sub> that is loaded only with Pt NPs, it shows a color of grey white. Unlike Ag and Au NPs with strong surface plasmon bands in the UV-vis region [56,57], TiO<sub>2</sub> supported Pt NPs exhibits increased and quite flat absorption of 68% over the whole range of 800–2500 nm, arising from the damping effect of the d-d transitions in Pt NPs which tends to wash out the free electron contribution to the dielectric function [58]. For the rGO-TiO<sub>2</sub>, the absorption significantly rises up to 94% for the long wavelength part of Vis-IR region, suggesting that the introduction of rGO into the matrix of rGO-TiO<sub>2</sub> is able to effectively promote the IR response of rGO-TiO<sub>2</sub> composites, which can be attributed to electronic interactions between rGO and TiO<sub>2</sub> [42] as well as reduced reflection of light [59]. For the hybrid Pt-rGO-TiO<sub>2</sub> of our research focus, its color becomes blue black and the absorption coefficient is further enhanced to 97% over IR light region due to the integrated effect of Pt NPs and rGO sheet. It is worth noting that all of the rGO-TiO<sub>2</sub> composites with different ratios of Pt

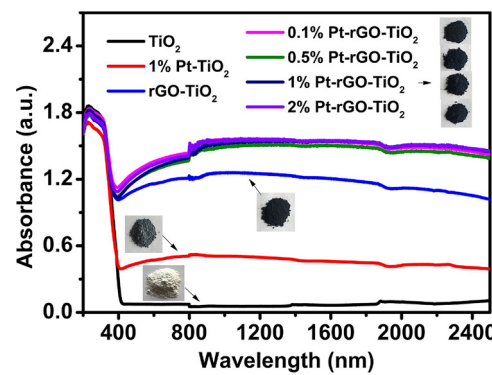
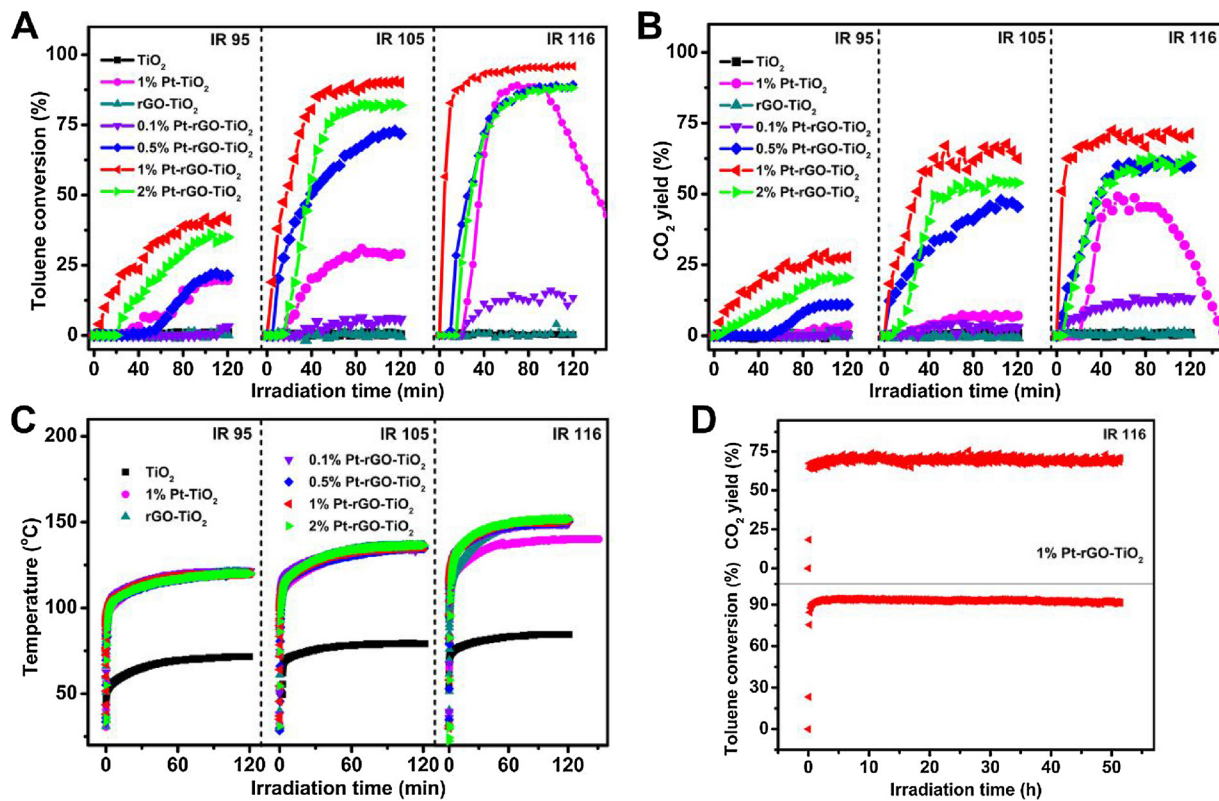


Fig. 2. UV-vis DRS of x% Pt-rGO-TiO<sub>2</sub> composites (x = 0, 0.1, 0.5, 1 and 2). 1% Pt-TiO<sub>2</sub> and TiO<sub>2</sub> is used for comparison.



**Fig. 3.** Time course of toluene conversion (A) and CO<sub>2</sub> yield (B) over  $\text{TiO}_2$ , 1% Pt-TiO<sub>2</sub> and x% Pt-rGO-TiO<sub>2</sub> (x = 0, 0.1, 0.5, 1 and 2) under IR irradiation with various light intensities (95, 106 and 116 mW/cm<sup>2</sup>); the temperature curve of the samples with their irradiation of IR lamp (C); the durability of 1% Pt-rGO-TiO<sub>2</sub> composites for toluene oxidation with IR irradiation of 116 mW/cm<sup>2</sup> under steady state conditions (D).

show high absorption with no significant difference, since the light absorption intensity of rGO is much stronger than Pt NPs. An ideal light absorber that a dark material absorbs radiation at all angles and polarizations [60], which demonstrates its possible potential as a suitable catalyst that efficiently absorbs light and releases the absorbed light energy in the form of heat (photo-thermal effect), resulting in a considerable increase of temperature, enough to stimulate thermocatalytic process. Thereby, Pt-rGO-TiO<sub>2</sub> catalysts can be expected to be as an efficient IR-light photon absorber to drive photo-thermal catalysis for a given reaction. This hypothesis is confirmed by the following gas-phase degradation of toluene over the Pt-rGO-TiO<sub>2</sub> composites under IR irradiation.

To confirm whether the broad IR absorption identified for Pt-rGO-TiO<sub>2</sub> composites is capable of driving solar energy conversion, we tested the catalytic activity of hybrid nanomaterial Pt-rGO-TiO<sub>2</sub> in the catalytic oxidation of gaseous toluene under IR light irradiation. The catalytic performance of the Pt-rGO-TiO<sub>2</sub> composites under IR lamp with different light intensities as a function of irradiation time is illustrated in Fig. 3(A) and (B). Remarkably, the conversion of toluene and the yield of CO<sub>2</sub> over Pt-rGO-TiO<sub>2</sub> composites increase with elevated light intensity from 95, 106 to 116 mW/cm<sup>2</sup>. The positive relationship between reaction conversions/CO<sub>2</sub> yields and light intensity can be explained by a photo-thermal effect, as a stronger light intensity results in a higher reaction temperature (Fig. 3(C) and Fig. S1), which is extremely favorable for endothermic reactions, i.e., catalytic oxidation of toluene. Under identical irradiation intensity, the photo-thermal catalytic performance for Pt-rGO-TiO<sub>2</sub> composites closely depends on the loading of Pt NPs. Specifically, the photo-thermal activity of these samples follows the sequence 1% Pt-rGO-TiO<sub>2</sub> > 2% Pt-rGO-TiO<sub>2</sub> ≥ 0.5% Pt-rGO-TiO<sub>2</sub> > 0.1% Pt-rGO-TiO<sub>2</sub>. Within 90 min of IR irradiation of 116 mW/cm<sup>2</sup>, the 1% Pt-rGO-TiO<sub>2</sub> composites shows the most active for photo-thermal catalytic degradation of toluene with the maximum conversion of 95% and CO<sub>2</sub> yield of 72%, which is obviously

higher than that achieved over 0.1% Pt-rGO-TiO<sub>2</sub>, 0.5% Pt-rGO-TiO<sub>2</sub> and 2% Pt-rGO-TiO<sub>2</sub> counterparts. In addition, it should be noted that among the 0.1% Pt-rGO-TiO<sub>2</sub>, 0.5% Pt-rGO-TiO<sub>2</sub>, 1% Pt-rGO-TiO<sub>2</sub> and 2% Pt-rGO-TiO<sub>2</sub> composites with uniform addition ratios of rGO, the reaction temperature for the photo-thermal activity is identical, that is, around 120, 135 and 150 °C when irradiated by IR light at the same intensity of 95, 106 and 116 mW/cm<sup>2</sup>, respectively. To get insight into the influence of Pt loading, the surface area analysis over Pt-rGO-TiO<sub>2</sub> composites has been performed and the results of N<sub>2</sub> adsorption-desorption isotherms are shown in Fig. S2. The BET surface areas of 0.1% Pt-rGO-TiO<sub>2</sub> composite is ca. 67.910 m<sup>2</sup> g<sup>-1</sup> and slightly decreases to 66.460 m<sup>2</sup> g<sup>-1</sup> and 65.615 m<sup>2</sup> g<sup>-1</sup> when the Pt loading is further increased from 0.1% to 0.5% and 1%, which are much higher than 57.485 m<sup>2</sup> g<sup>-1</sup> of 2% Pt-rGO-TiO<sub>2</sub> composite. The large specific surface area, in most case, could afford abundant active sites for gas absorption and behave as an important reason for the enhanced catalytic activities [61], but in this work, it is not a decisive factor, since the results of specific surface area are inconsistent with photo-thermal catalytic activities. In the previous study of Zhang's group [62] that the MnCeW/m-TiO<sub>2</sub> catalyst had the smallest specific surface area of 96 m<sup>2</sup> g<sup>-1</sup> in comparison with MnCe/m-TiO<sub>2</sub>, MnW/m-TiO<sub>2</sub> and Mn/m-TiO<sub>2</sub> counterparts, but exhibited the best catalytic performance for NO<sub>x</sub> reduction owing to the promotional effects of W. Furthermore, the toluene adsorption experiment was performed and the result in Fig. S3 shows that the 1% Pt-rGO-TiO<sub>2</sub> composite exhibits the strongest adsorption capability toward reactant, possibly being associated with well dispersed Pt NPs on the 2D rGO sheet and large amount of exposed active Pt sites. Because the heterogeneous photo-thermal catalysis is a surface-based redox process [63], the high adsorption capacity over 1% Pt-rGO-TiO<sub>2</sub> enables the surface lattice oxygen to effectively react with toluene adsorbed on the surface of catalyst, which, in turn, contributes to the catalytic activity enhancement. The synergistic effects of these factors would lead to the higher photo-thermal efficiency of 1% Pt-rGO-TiO<sub>2</sub>.

composite than that of the 0.1% Pt-rGO-TiO<sub>2</sub>, 0.5% Pt-rGO-TiO<sub>2</sub> and 2% Pt-rGO-TiO<sub>2</sub> counterparts. To further demonstrate the advantages of the 1% Pt-rGO-TiO<sub>2</sub> composites in photo-thermal catalysis, the contrast reactions over TiO<sub>2</sub>, rGO-TiO<sub>2</sub> and 1% Pt-TiO<sub>2</sub> were also performed. The results show that no observable catalytic activities for either the bare TiO<sub>2</sub> or the rGO-TiO<sub>2</sub> composites under IR irradiation are demonstrated, because neither IR light can be absorbed in pure TiO<sub>2</sub> nor active sites can be provided in rGO-TiO<sub>2</sub> composites. Remarkably, under IR irradiation, the 1% Pt-rGO-TiO<sub>2</sub> catalyst shows almost complete conversion of toluene at light intensity of 116 mW/cm<sup>2</sup>, while that of 1% Pt-TiO<sub>2</sub> decreased by 7% under identical reaction conditions. It should be noted especially that the stability of 1% Pt-TiO<sub>2</sub> catalyst, which gave a gradual climbing curve of toluene conversion and CO<sub>2</sub> yield, and reaching to maximum at ca. 88% and 45% for about 90 min, then gradually decreased to 44% and 9% with the irradiation time further increased to 150 min. More significantly, the stability experiment of 1% Pt-rGO-TiO<sub>2</sub> composite clearly shows that the toluene conversion and CO<sub>2</sub> yield are close to 95% and 72% over consecutive irradiation of 50 h in Fig. 3(D).

Severe deactivation of 1% Pt-TiO<sub>2</sub> catalyst during the catalytic oxidation of toluene was also reported in previous literatures [64,65], where the inactivation mainly originates from the accumulation of partially oxidized intermediates, such as benzyl alcohol, benzaldehyde and benzoic acid, which more strongly adsorbs on TiO<sub>2</sub> surface than toluene to occupy the active sites on the catalyst surface. The activity experiment result in Fig. 3(B) displays that the mineralization of toluene on 1% Pt-TiO<sub>2</sub> catalyst occurs slowly with accumulating recalcitrant intermediates, which is closely related to deactivation, whereas the oxidation reaction efficiently boosts the mineralization efficiency of toluene over the 1% Pt-rGO-TiO<sub>2</sub> composite to inhibit the deposition of recalcitrant intermediates on the catalyst surface, which consequently increases the durability of catalyst. The significant difference of reaction durability between 1% Pt-TiO<sub>2</sub> and 1% Pt-rGO-TiO<sub>2</sub> composites can be attributed to a promotional effect of rGO nanosheet. The BET surface area of 1% Pt-rGO-TiO<sub>2</sub> composite is ca. 65.615 m<sup>2</sup> g<sup>-1</sup>, which is higher than 58.545 m<sup>2</sup> g<sup>-1</sup> of 1% Pt-TiO<sub>2</sub>, since the rGO sheets contribute to increase the specific surface area of rGO-based composites. Moreover, the toluene-TPD experiment result in Fig. 4 shows that 1% Pt-rGO-TiO<sub>2</sub> exhibits stronger adsorption capability toward reactant than 1% Pt-TiO<sub>2</sub>, because rGO has a strong affinity to toluene molecules involving the increased intermolecular  $\pi$ - $\pi$  interaction with expanding  $\pi$ -conjugation [66,67]. Furthermore, the well-dispersed Pt NPs in 1% Pt-rGO-TiO<sub>2</sub> leads to higher density of chemisorbed reactant and larger amount of exposed active sites for the quick surface toluene mineralization over 1% Pt-rGO-TiO<sub>2</sub> than those over 1% Pt-TiO<sub>2</sub> [68], as well as its strong photo-thermal effect giving rise to the unique ability against catalyst deactivation and the excellent reaction stability of 1% Pt-rGO-TiO<sub>2</sub> composite for toluene oxidation.

Furthermore, the microscopic structure of Pt, TiO<sub>2</sub> NPs with rGO in

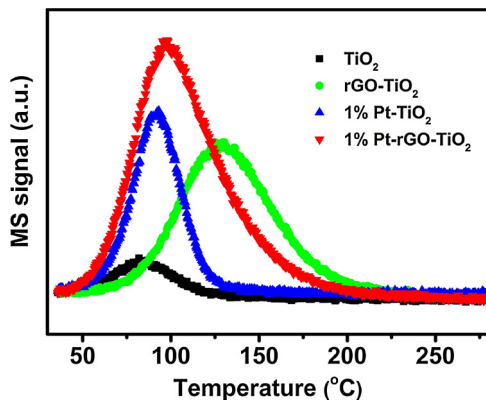
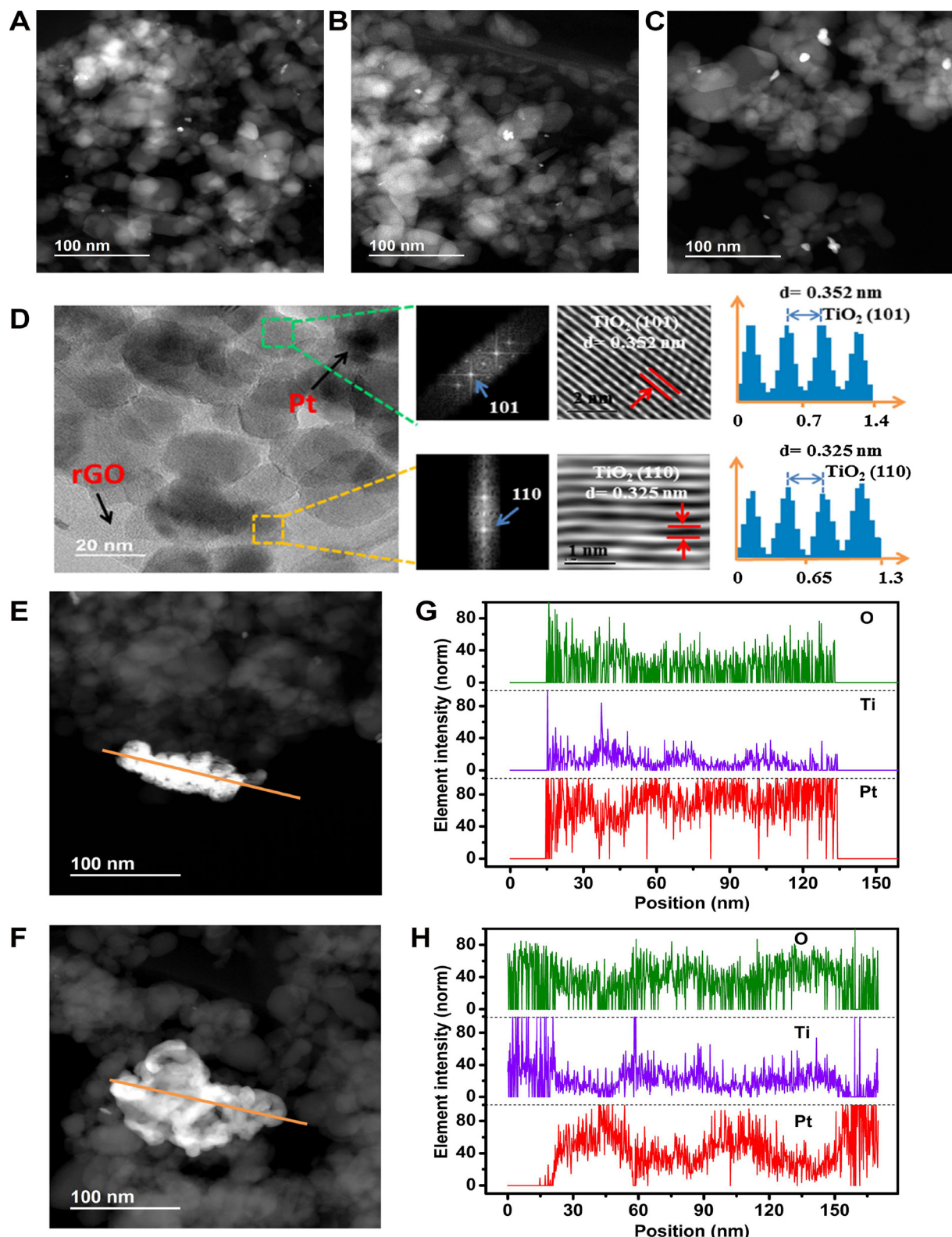


Fig. 4. Toluene-TPD of TiO<sub>2</sub>, rGO-TiO<sub>2</sub>, 1% Pt-TiO<sub>2</sub> and 1% Pt-rGO-TiO<sub>2</sub>.

Pt-rGO-TiO<sub>2</sub> was characterized by HR-TEM. As shown in Fig. 5(D) and Fig. S4, rGO sheet exhibits extremely thin morphology with ripples, which could increase the surface area to support Pt-TiO<sub>2</sub> NPs and provide good potential for light absorption (Table 1) [71]. Additionally, Pt NPs are either uniformly dispersed on the surface of rGO sheet in isolation or stuck with TiO<sub>2</sub> on rGO sheet. The fast Fourier transform (FFT) patterns of the selected area (marked by the green and yellow frame) shown in Fig. 5(D) authenticate the anatase nanocrystals with 0.351 nm lattice spacing of (101) facet and rutile nanocrystals with 0.325 nm lattice spacing of (110) facet. HAADF-STEM was further performed to confirm the distribution and configuration of Pt. The STEM and HR-TEM images of 2% Pt-rGO-TiO<sub>2</sub> and 1% Pt-TiO<sub>2</sub> (Fig. 5(E, F) and Fig. S4) show the severe agglomeration of Pt NPs, with the identity of these agglomerates confirmed by strong signals of Pt in a EDS line scan of Fig. 5(G, H) and EDS spectrum of Fig. S4(G, H). This reveals that the rGO sheet protects Pt NPs to maintain their original size/morphology when the Pt NPs with 1 wt % loading or below. That is, the introduction of rGO sheet efficiently inhibits the agglomeration of Pt NPs in Pt-rGO-TiO<sub>2</sub> composites, which can improve the utilization efficiency of Pt NPs, light absorption and reactant adsorptivity to accelerate the photo-thermal catalytic reaction. By the way, the aforementioned comparison characterizations evidence that (1) the optical property as well as the crystal phase of the catalysts almost kept unchanged after different amount of Pt loading, confirmed by the DRS and XRD observations; (2) the synergistic effects of high adsorption capacity, well dispersed supported Pt-TiO<sub>2</sub> catalyst on the 2D rGO sheet and large amount of exposed active Pt sites are the decisive factors for the excellent performance of Pt-rGO-TiO<sub>2</sub> composites rather than the slight change in specific surface area.

To understand if the high catalytic activity of 1% Pt-rGO-TiO<sub>2</sub> under IR irradiation arises from the photocatalysis and/or photo-thermocatalysis, the photocatalytic activity of 1% Pt-rGO-TiO<sub>2</sub> composite for toluene oxidation was carried out. 100 mg of 1% Pt-rGO-TiO<sub>2</sub> was coated on a cylindrical quartz reactor (5 cm × 5 cm × 1 cm) and then the reactor was placed in a glycerol-water bath of ultralow temperature (−20 °C) to ensure the photocatalytic reaction at near room temperature (28 °C) under IR irradiation of 116 mW/cm<sup>2</sup>. However, in this case, neither distinct photo-degradation of toluene nor the discernable generation of CO<sub>2</sub> can be clearly observed in Fig. S5(A). This indicates that the 1% Pt-rGO-TiO<sub>2</sub> composite is photocatalytically inert toward the oxidation of toluene under IR light at room temperature, which can be attributed mainly to (1) wide-bandgap TiO<sub>2</sub>(A) and TiO<sub>2</sub>(R) [72], not being able to be activated by the inadequate excitation energy of IR photon, (2) the zero bandgap of graphene [73] (Fig. S5(B)) endowed the holes in the composites with inadequate oxidation capacity and ineffective transfer to the VB of either TiO<sub>2</sub>(A) or TiO<sub>2</sub>(R) due to the stringent valence-band position requirement of semiconductor catalysts, and (3) inexistence of energetic hot holes injection from the excitation of Pt NPs with broad light absorption without recognizable peaks (Fig. S5(C)) [74]. Notably, the strong and anisotropic bonding and the low mass of the carbon atoms give graphene and graphene-based materials unique thermal properties, where graphene as nanometer-sized heaters can strongly absorb NIR light and effectively convert it into thermal energy to raise the temperature of composites [75–79]. Impressively, the temperature of rGO-TiO<sub>2</sub> and x% Pt-rGO-TiO<sub>2</sub> composites quickly increases from room temperature to 120 °C, 135 °C and 150 °C with the lamp on the light intensity of 95, 106, 116 mW/cm<sup>2</sup>, respectively. When the temperature reaches a plateau, an equilibrium is established between the absorption of light energy and the energy dissipation from the catalyst to the surroundings [80]. The plateau temperatures of the catalysts demonstrate direct evidence for their efficient photo-thermal conversion. For high photo-thermal energy conversion efficiency, it is a prerequisite for an ideal material to markedly absorb IR light, efficiently convert the harvested photon into heat thermal energy and provide effective catalytic active sites. The 1% Pt-rGO-TiO<sub>2</sub> composite, featuring the broad light wavelength



**Fig. 5.** High-angle annular dark-field scanning transmission electron microscopy (HAADF-STEM) images and HRTEM of  $x\%$  Pt-rGO-TiO<sub>2</sub> ( $x = 0.1$  (A),  $0.5$  (B),  $1$  (C-D) and  $2$  (E)) and  $1\%$  Pt-TiO<sub>2</sub> (F), (the right side of (D) is the fast Fourier transform (FFT) pattern of the area marked by the green and yellow square box and the corresponding intensity profiles); Energy dispersive X-ray spectroscopy (EDS) line scan line mapping profiles of (G)  $2\%$  Pt-rGO-TiO<sub>2</sub> and (H)  $1\%$  Pt-TiO<sub>2</sub> along the directions marked by the orange lines in (E) and (F), respectively (For interpretation of the references to colour in this figure legend, the reader is referred to the web version of this article).

**Table 1**  
Physical structural parameters of various samples.

Entry	Absorptance (%) <sup>a</sup>	$S_{\text{BET}}$ ( $\text{m}^2 \text{g}^{-1}$ )	Pore volume ( $\text{cm}^3 \text{g}^{-1}$ )	Mean size of Pt NPs (nm) <sup>b</sup>	Pt loading (wt%) <sup>c</sup>
IR ( $800 \leq \lambda \leq 2500 \text{ nm}$ )					
TiO <sub>2</sub>	0	53.476	0.433	/	/
1% Pt-TiO <sub>2</sub>	67.672	58.545	0.480	part aggregated	1.10
rGO-TiO <sub>2</sub>	93.985	72.510	0.481	/	/
0.1% Pt-rGO-TiO <sub>2</sub>	97.116	67.910	0.463	3.6	0.09
0.5% Pt-rGO-TiO <sub>2</sub>	96.701	66.460	0.459	4.1	0.44
1% Pt-rGO-TiO <sub>2</sub>	96.934	65.615	0.457	4.8	0.91
2% Pt-rGO-TiO <sub>2</sub>	97.091	57.485	0.486	part aggregated	1.86

<sup>a</sup> Absorptance ( $a = \int (1-R(\lambda)) \cdot E_{\text{IR}} / \int E_{\text{IR}}$ ) [69,70].

<sup>b</sup> Mean size of Pt NPs was analyse from STEM.

<sup>c</sup> Bulk composition was measured by ICP-OES.

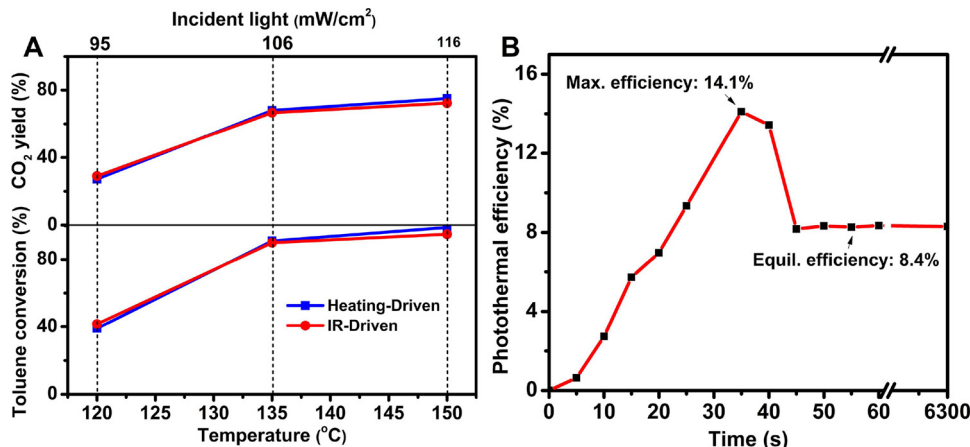


**Fig. 6.** The toluene conversion and CO<sub>2</sub> yield over 1% Pt-rGO-TiO<sub>2</sub> composites under IR irradiation with different light intensities at 90 min or upon heating at corresponding temperatures (A); photo-thermal conversion efficiency of 1% Pt-rGO-TiO<sub>2</sub> composites under IR irradiation of 116 mW/cm<sup>2</sup> (B).

absorption, exhibits a strong IR heating effect with a considerable increase of local temperature in the catalyst and surrounding medium, which was expected to trigger and accelerate chemical reactions nearby. To further determine whether the high catalytic activity observed with 1% Pt-rGO-TiO<sub>2</sub> composite is induced by the photo-thermal effect, the thermocatalytic activity for toluene oxidation was performed in a cylindrical stainless steel reactor at different temperatures by external electrical heating and monitored on an online gas-phase chromatograph. As shown in Fig. 6(A), the toluene conversion and the CO<sub>2</sub> yield of 1% Pt-rGO-TiO<sub>2</sub> composite achieved by heating at the temperatures of 120, 135 and 150 °C are similar to those obtained by IR irradiation of 95, 106 and 116 mW/cm<sup>2</sup>, respectively. These results imply that the efficient infrared light promoted degradation of toluene over photo-thermal responsive 1% Pt-rGO-TiO<sub>2</sub> composite should be closely associated with the photo-thermocatalysis. The photo-thermal conversion efficiency ( $\eta$ ) is defined as the ratio of the converted thermal energy to the incident light energy [81] where the maximum efficiency and equilibrium efficiency reach 14.1% and 8.4% for 1% Pt-rGO-TiO<sub>2</sub> composite under IR irradiation of 116 mW/cm<sup>2</sup>, respectively, which is shown in Fig. 6(B).

The mechanism that the oxidation of a given VOCs depends on activated forms of oxygen, *i.e.*, lattice oxygen and adsorbed oxygen [82]. To further investigate the adsorption and activation of oxygen on 1% Pt-rGO-TiO<sub>2</sub> composite, as well as the lattice oxygen mobility of the catalyst, O<sub>2</sub>-TPD measurement was performed. As shown in Fig. 7(A), 1% Pt-rGO-TiO<sub>2</sub> composite displays a large intense peak at around 490 °C and a small sharp peak centered at around 679 °C, corresponding to the surface lattice oxygen species O<sub>2</sub><sup>-</sup>, while the peaks below 400 °C and above 700 °C are assigned to surface adsorbed peroxy species O<sub>2</sub><sup>-</sup>/monatomic species O<sup>-</sup> and bulk lattice oxygen, respectively [83,84]. Notably, for the O<sub>2</sub><sup>-</sup> lattice desorption, 1% Pt-rGO-TiO<sub>2</sub> composites

revealed a much stronger intensity than either hybrid 1% Pt-TiO<sub>2</sub> or TiO<sub>2</sub> NPs, indicating that the desorption amount of surface lattice oxygen species of the 1% Pt-rGO-TiO<sub>2</sub> catalyst are greatly enhanced. Morales et al. [85] previously suggested that the adsorbed oxygen on the catalyst surface released at low temperature participates in the surface oxidation reaction via a Rideal-Eley mechanism, while lattice oxygen of the catalyst with high oxygen mobility is desorbed at high temperature ( $> 400$  °C) and proceeds the redox cycle via a Mars-van Krevelen mechanism. Meanwhile, it has been widely believed that VOC oxidation over reducible transition-metal oxides such as TiO<sub>2</sub>, WO<sub>3</sub>, CeO<sub>2</sub>, etc, follows a Mars-van Krevelen mechanism [86]. The key characteristic feature of this mechanism is that the oxide surface is directly involved via its most reactive surface lattice oxygen atoms, rather than just a spectator of the reaction. In the research of Li and co-workers [87], the experimental data strongly support a typical Mars-van Krevelen type mechanism for benzene oxidation reaction by investigating the evolution of CO<sub>2</sub> concentration in the atmosphere of highly pure Ar after the injection of benzene into the reactor with the TiO<sub>2</sub> catalyst during either photo-thermal or thermal catalytic process. Recently, DRIFTS experiment performed by Maier's research group [88] also support this mechanism that the formation of carboxylates in oxygen-free feed gas manifests that propane is not activated by pre-adsorbed oxygen, but by the TiCrO<sub>x</sub> catalyst itself. To further validate whether or not a similar dynamic adatom mechanism is also feasible on 1% Pt-rGO-TiO<sub>2</sub> composite, *in situ* DRIFTS spectroscopy was applied to look into the effect of surface lattice oxygen on toluene oxidation reactivity [89]. Prior to toluene adsorption and reaction experiments, the sample was flushed with pure N<sub>2</sub> at 150 °C for 1.5 h to remove adsorbed impurities. The background spectrum was collected under N<sub>2</sub> and automatically deducted from the sample spectra. Afterward, 1000 ppm toluene/N<sub>2</sub> was introduced to the cell at a flow rate of 50 mL/min at

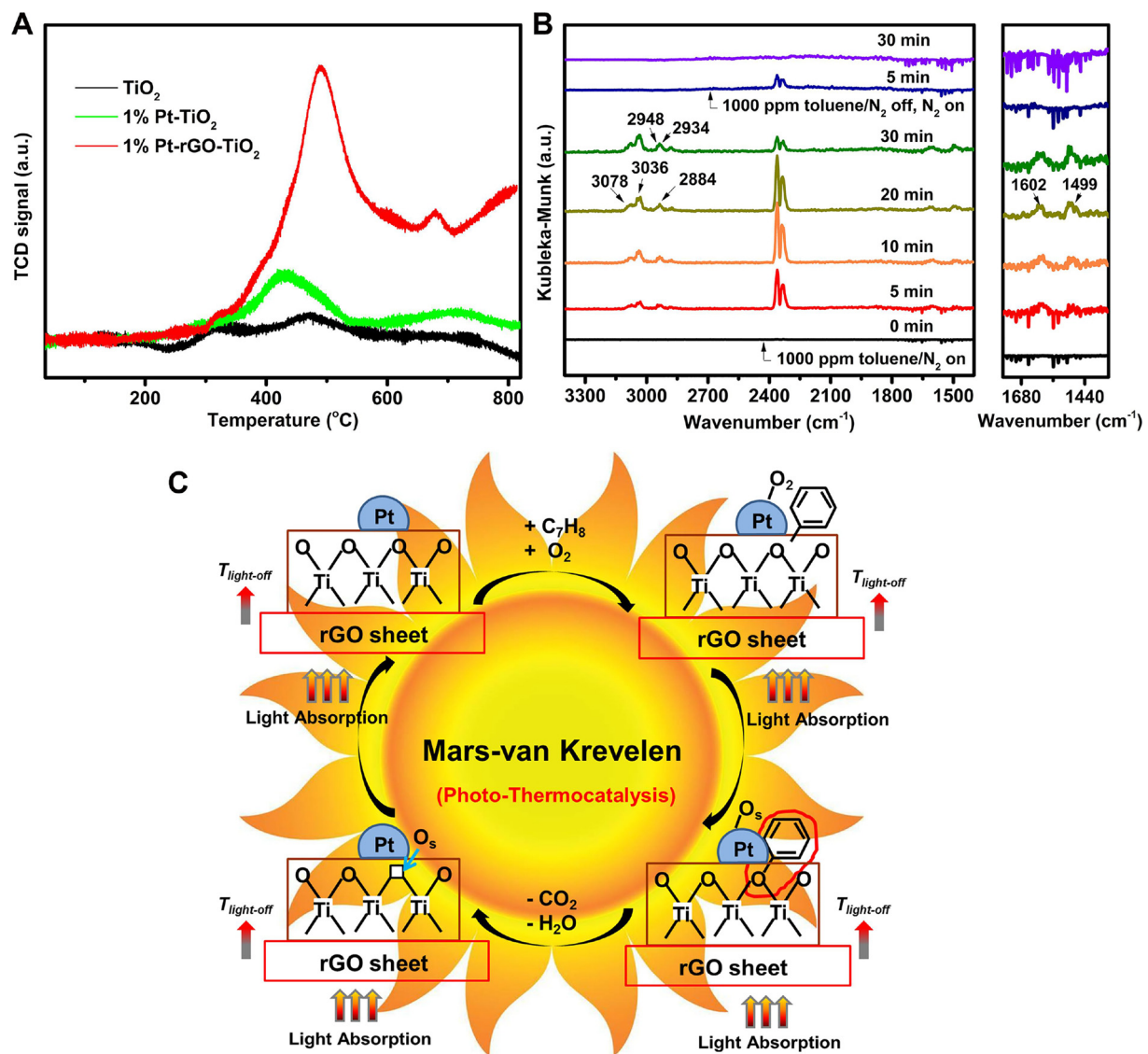


**Fig. 7.** O<sub>2</sub>-TPD profiles of the TiO<sub>2</sub>, 1% Pt-TiO<sub>2</sub> and 1% Pt-rGO-TiO<sub>2</sub> composites (A); *in situ* DRIFTS spectra of species on 1% Pt-rGO-TiO<sub>2</sub> composites for the adsorption of toluene in N<sub>2</sub> upon heating at 150 °C (B), the right side of (B) is the enlarged view at 1750–1350 cm<sup>-1</sup>; schematic diagram of the proposed Pt-assisted Mars-van Krevelen mechanism of photo-thermal catalysis (C).

150 °C, and then DRIFTS spectra were recorded. The DRIFTS spectra of 1% Pt-rGO-TiO<sub>2</sub> composite in Fig. 7(B) show that the broad peaks at 3078 and 3036 cm<sup>-1</sup> are characteristic of C–H stretching vibrations of the aromatic ring. The strong peaks located at 2948, 2934, 2884 cm<sup>-1</sup> and 1602, 1499 cm<sup>-1</sup> are associated with asymmetric/symmetric C–H stretching vibrations of methyl group and in-plane skeletal vibration of the aromatic ring [90], respectively, which originates from the adsorbed toluene. Noticeably, the new weak bands at 1630 and 1383 cm<sup>-1</sup> assigned to various vibrations of the aromatic ring/methyl/carboxyl groups and the asymmetric/symmetric vibrations of COO group observably appear, resulting from the oxidation of the breaking methyl or ring [90]. These band intensities monotonically increase with time on stream, revealing that organic byproducts are accumulated on the catalyst surface. Moreover, the new doublet peaks attributable to asymmetric O=C=O stretching vibrations at 2367 and 2339 cm<sup>-1</sup> are clearly observed [91,92], while the generated CO<sub>2</sub> arises from the deep oxidation of the carboxylate species. Obviously, the intensity of the bands assigned to CO<sub>2</sub> linearly increases with time on stream during the first 20 min, which implies that the oxidation of toluene proceeds even in oxygen-free feed gas. Moreover, the involvement of adsorbed oxygen or gaseous oxygen in the activation of toluene is completely excluded,

which confirms that lattice oxygen is involved in the deep catalytic oxidation of toluene on 1% Pt-rGO-TiO<sub>2</sub> composite. Furthermore, adsorbed toluene could be oxidized on the catalyst surface, thereby giving rise to carboxylate intermediates [93]. The formation of carboxylate intermediates and CO<sub>2</sub> end-product in oxygen-free feed gas suggest that toluene is activated by the 1% Pt-rGO-TiO<sub>2</sub> catalyst itself. Additionally, the flow of N<sub>2</sub> was introduced to replace 1000 ppm toluene/N<sub>2</sub> to further investigate the reactivity at 150 °C. The adsorbed toluene reactant and accumulated intermediate carbonate species at extended reaction times continue to react with lattice oxygen, thereby these bands assigned to toluene and carbonate species disappear and the bands corresponding to CO<sub>2</sub> still exist. Based on the O<sub>2</sub>-TPD and DRIFTS observations, we can conclude that under oxygen free condition, the surface lattice oxygen from 1% Pt-rGO-TiO<sub>2</sub> composite can actively react with adsorbed toluene via a Mars-van Krevelen mechanism to generate intermediate carboxylate species and end-product CO<sub>2</sub>. Upon IR irradiation, photo-thermal responsive 1% Pt-rGO-TiO<sub>2</sub> composite achieves broad spectrum utilization for thermalization and then rGO via phonon-phonon coupling resulting in heat dissipation into the surrounding medium. The heat generated is used to increase the local temperature of the system, thereby driving the toluene catalytic

oxidation reaction via a Pt-assisted Mars-van Krevelen mechanism. On the 1% Pt-rGO-TiO<sub>2</sub> catalyst, the adsorbed toluene can pick up surface lattice oxygen atoms located at low-coordinated sites on the TiO<sub>2</sub> surface to form the oxygenated compound (i.e. CO<sub>2</sub>, H<sub>2</sub>O), simultaneously leaving behind oxygen vacancies on the surface where metal oxide TiO<sub>2</sub> lose oxygen atoms and donate them to the adsorbed toluene in the process [86]. In order to realize the persistent catalytic activity, the reaction must take place under oxygen pressure so that molecular oxygen dissociatively adsorbed onto the Pt NPs to give surface oxygen adatoms then followed a spillover of the oxygen adatoms from Pt NPs to the surface of the TiO<sub>2</sub> to refill the vacancies created in the oxidative process [94], which resulted in the efficient catalytic oxidation of toluene. The schematic of the proposed Pt-assisted Mars-van Krevelen mechanism of the photo-thermal catalysis is shown in Fig. 7(C).

#### 4. Conclusions

In summary, the utilization of renewable solar energy via infrared light photo-thermocatalysis is seen to offer a potential alternative strategy for environmental remediation. The restacking-inhibited 2D rGO sheet, featuring the broad IR light absorption, results in efficient light-to-heat conversion, enhanced adsorption capacity and well dispersed supported Pt-TiO<sub>2</sub> catalyst, thereby increasing reaction temperature above light-off temperature for driving photo-thermocatalytic redox reactions. Under infrared irradiation with low power density (116 mW/cm<sup>2</sup>), photo-thermal responsive 1% Pt-rGO-TiO<sub>2</sub> composite demonstrates excellent catalytic activity with 95% of toluene conversion and 72% of CO<sub>2</sub> yield, along with retaining its stability for nearly 50 h, in which the maximum photo-thermal conversion efficiency is able to reach 14.1%. These results highlight the achievement of graphene-based composites as IR light photon absorber to trigger redox reactions, which will open an attractive avenue to harvesting solar light through photo-thermal effect. It is anticipated that this work may enable the wide development of graphene-based composites photo-thermocatalysis for solar energy conversion.

#### Acknowledgements

This work was supported by the Nature Science Foundation of Fujian Province of China [No. 2016J01079, No. 2016J05049], the One Hundred Talent Project and the Key Program for Frontier Sciences-Youth Scientist from Chinese Academy of Sciences [QYZDB-SSW-DQC022], the National Natural Science Foundation of China [No. 21501175, No. 21703233], the key project of National Natural Science Foundation of China [U1463204] and the Natural Science Foundation (NSF) of Fujian Province for Distinguished Young Investigator Rolling Grant [2017J07002].

#### Appendix A. Supplementary data

Supplementary material related to this article can be found, in the online version, at doi:<https://doi.org/10.1016/j.apcatb.2018.04.011>.

#### References

- A.K. Sinha, K. Suzuki, Three-dimensional mesoporous chromium oxide: a highly efficient material for the elimination of volatile organic compounds, *Angew. Chem. Int. Ed.* 44 (2005) 271–273.
- L.F. Liotta, Catalytic oxidation of volatile organic compounds on supported noble metals, *Appl. Catal. B-Environ.* 100 (2010) 403–412.
- P. Christopher, H. Xin, S. Linic, Visible-light-enhanced catalytic oxidation reactions on plasmonic silver nanostructures, *Nat. Chem.* 3 (2011) 467–472.
- N. Armaroli, V. Balzani, The future of energy supply: challenges and opportunities, *Angew. Chem. Int. Ed.* 46 (2007) 52–66.
- Y.H. Ng, S. Ikeda, M. Matsumura, R. Amal, A perspective on fabricating carbon-based nanomaterials by photocatalysis and their applications, *Energy Environ. Sci.* 5 (2012) 9307–9318.
- X.Z. Zheng, L.W. Zhang, Photonic nanostructures for solar energy conversion, *Energy Environ. Sci.* 9 (2016) 2511–2532.
- J.L. Long, H.J. Chang, Q. Gu, J. Xu, L.Z. Fan, S.C. Wang, Y.G. Zhou, W. Wei, L. Huang, X.X. Wang, P. Liu, W. Huang, Gold-plasmon enhanced solar-to-hydrogen conversion on the {001} facets of anatase TiO<sub>2</sub> nanosheets, *Energy Environ. Sci.* 7 (2014) 973–977.
- J.L. Zhang, Y.M. Wu, M.Y. Xing, S.A.K. Leghari, S. Sajjad, Development of modified N doped TiO<sub>2</sub> photocatalyst with metals, nonmetals and metal oxides, *Energy Environ. Sci.* 3 (2010) 715–726.
- Z. Shayegan, C.-S. Lee, F. Haghagh, TiO<sub>2</sub> photocatalyst for removal of volatile organic compounds in gas phase - a review, *Chem. Eng. J.* 334 (2018) 2408–2439.
- L.X. Zhong, J.J. Branco, S. Batterman, B.M. Bartlett, C. Godwin, Experimental and modeling study of visible light responsive photocatalytic oxidation (PCO) materials for toluene degradation, *Appl. Catal. B-Environ.* 216 (2017) 122–132.
- B.Y. Xu, Y. An, Y.Y. Liu, X.Y. Qin, X.Y. Zhang, Y. Dai, Z.Y. Wang, P. Wang, M.H. Whangbo, B. Huang, Enhancing the photocatalytic activity of BiOX (X = Cl, Br, and I), (BiO)<sub>x</sub>CO<sub>3</sub> and Bi<sub>2</sub>O<sub>3</sub> by modifying their surfaces with polar organic anions, 4-substituted thiophenolates, *J. Mater. Chem. A* 5 (2017) 14406–14414.
- D.M. Schultz, T.P. Yoon, Solar synthesis: prospects in visible light photocatalysis, *Science* 343 (2014) 1239176–1239183.
- Y.H. Sang, Z.H. Zhao, M.W. Zhao, P. Hao, Y.H. Leng, H. Liu, From UV to near-infrared, WS<sub>2</sub> nanosheet: a novel photocatalyst for full solar light spectrum photodegradation, *Adv. Mater.* 27 (2015) 363–369.
- C.H. Li, F. Wang, J.A. Zhu, J.C. Yu, NaYF<sub>4</sub> Yb,Tm/CdS composite as a novel near-infrared-driven photocatalyst, *Appl. Catal. B-Environ.* 100 (2010) 433–439.
- W. Wang, W.J. Huang, Y.R. Ni, C.H. Lu, Z.Z. Xu, Different upconversion properties of beta-NaYF<sub>4</sub>:Yb<sup>3+</sup>,Tm<sup>3+</sup>/Er<sup>3+</sup> in affecting the near-infrared-driven photocatalytic activity of high-reactive TiO<sub>2</sub>, *ACS Appl. Mater. Interfaces* 6 (2014) 340–348.
- M. Chatti, V. Adusumalli, S. Ganguli, V. Mahalingam, Near-infrared light triggered superior photocatalytic activity from MoS<sub>2</sub>-NaYF<sub>4</sub>:Yb<sup>3+</sup>/Er<sup>3+</sup> nanocomposites, *Dalton Trans.* 45 (2016) 12384–12392.
- S. Wu, H.J. Butt, Near-infrared-sensitive materials based on upconverting nanoparticles, *Adv. Mater.* 28 (2016) 1208–1226.
- W.N. Wang, F. Zhang, C.L. Zhang, Y.C. Guo, W. Dai, H.S. Qian, Fabrication of zinc oxide composite microfibers for near-infrared-light-mediated photocatalysis, *ChemCatChem* 9 (2017) 3611–3617.
- L.M. Wang, X.Y. Li, Z.Q. Li, W.S. Chu, R.F. Li, K. Lin, H.S. Qian, Y. Wang, C.F. Wu, J. Li, D.T. Tu, Q. Zhang, L. Song, J. Jiang, X.Y. Chen, Y. Luo, Y. Xie, Y.J. Xiong, A new cubic phase for a NaYF<sub>4</sub> host matrix offering high upconversion luminescence efficiency, *Adv. Mater.* 27 (2015) 5528–5533.
- J. Tian, Y.H. Sang, G.W. Yu, H.D. Jiang, X.N. Mu, H. Liu, A Bi<sub>2</sub>WO<sub>6</sub>-based hybrid photocatalyst with broad spectrum photocatalytic properties under UV-vis, and near-infrared irradiation, *Adv. Mater.* 25 (2013) 5075–5080.
- H.T. Li, R.H. Liu, Y. Liu, H. Huang, H. Yu, H. Ming, S.Y. Lian, S.T. Lee, Z.H. Kang, Carbon quantum dots/Cu<sub>2</sub>O composites with protruding nanostructures and their highly efficient (near) infrared photocatalytic behavior, *J. Mater. Chem.* 22 (2012) 17470–17475.
- J. Tian, Y.H. Sang, Z.H. Zhao, Y. Xia, Y.H. Sang, P. Hao, J. Zhan, M.C. Li, H. Liu, Carbon quantum dots/hydrogenated TiO<sub>2</sub> nanobelt heterostructures and their broad spectrum photocatalytic properties under UV-vis, and near-infrared irradiation, *Nano Energy* 11 (2015) 419–427.
- J. Zhang, C.M. Shadé, D.A. Chengelis, S. Petoud, A strategy to protect and sensitize near-infrared luminescent Nd<sup>3+</sup> and Yb<sup>3+</sup>: organic tropolone ligands for the sensitization of Ln<sup>3+</sup>-doped NaYF<sub>4</sub> nanocrystals, *J. Am. Chem. Soc.* 129 (2007) 14834–14835.
- Z.J. Zhang, W.Z. Wang, Infrared-light-induced photocatalysis on BiErWO<sub>6</sub>, *Dalton Trans.* 42 (2013) 12072–12074.
- G. Wang, B.B. Huang, X.C. Ma, Z.Y. Wang, X.Y. Qin, X.Y. Zhang, Y. Dai, M.H. Whangbo, Cu<sub>2</sub>(OH)PO<sub>4</sub>, a near-infrared-activated photocatalyst, *Angew. Chem. Int. Ed.* 52 (2013) 4810–4813.
- Q. Zhang, Y. Zhou, Z. Zhang, Y. He, Y.D. Chen, Y.H. Lin, Plasmonic photocatalyst, *Prog. Chem.* 25 (2013) 2020–2027.
- Z. Wang, C.Y. Yang, T.Q. Lin, H. Yin, P. Chen, D.Y. Wan, F.F. Xu, F.Q. Huang, J.H. Lin, X.M. Xie, M.H. Jiang, H-doped black titania with very high solar absorption and excellent photocatalysis enhanced by localized surface plasmon resonance, *Adv. Funct. Mater.* 23 (2013) 5444–5450.
- W.B. Hou, S.B. Cronin, A review of surface plasmon resonance-enhanced photocatalysis, *Adv. Funct. Mater.* 23 (2013) 1612–1619.
- S.K. Cushing, A.D. Bristow, N.Q. Wu, Theoretical maximum efficiency of solar energy conversion in plasmonic metal-semiconductor heterojunctions, *Phys. Chem. Chem. Phys.* 17 (2015) 30013–30022.
- J.B. Cui, Y.J. Li, L. Liu, L. Chen, J. Xu, J.W. Ma, G. Fang, E.B. Zhu, H. Wu, L.X. Zhao, L.Y. Wang, Y. Huang, Near-infrared plasmonic-enhanced solar energy harvest for highly efficient photocatalytic reactions, *Nano Lett.* 15 (2015) 6295–6301.
- X.H. Huang, I.H. El-Sayed, W. Qian, M.A. El-Sayed, Cancer cell imaging and photothermal therapy in the near-infrared region by using gold nanorods, *J. Am. Chem. Soc.* 128 (2006) 2115–2120.
- A.M. Gobin, E.M. Watkins, E. Quevedo, V.L. Colvin, J.L. West, Near-infrared-resonant gold/gold sulfide nanoparticles as a photothermal cancer therapeutic agent, *Small* 6 (2010) 745–752.
- J.Y. Chen, D.L. Wang, J.F. Xi, L. Au, A. Siekkinen, A. Warsen, Z.Y. Li, H. Zhang, Y.N. Xia, X.D. Li, Immuno gold nanocages with tailored optical properties for targeted photothermal destruction of cancer cells, *Nano Lett.* 7 (2007) 1318–1322.
- J. Hu, H. Wang, F. Dong, Z. Wu, A new strategy for utilization of NIR from solar energy-promotion effect generated from photothermal effect of Fe<sub>3</sub>O<sub>4</sub>@SiO<sub>2</sub> for photocatalytic oxidation of NO, *Appl. Catal. B-Environ.* 204 (2017) 584–592.
- X. Huang, X.Y. Qi, F. Boey, H. Zhang, Graphene-based composites, *Chem. Soc. Rev.* 35 (2016) 103–138.

41 (2012) 666–686.

[36] Q.J. Xiang, J.G. Yu, M. Jaroniec, Graphene-based semiconductor photocatalysts, *Chem. Soc. Rev.* 41 (2012) 782–796.

[37] N. Zhang, M.Q. Yang, S.Q. Liu, Y.G. Sun, Y.J. Xu, Waltzing with the versatile platform of graphene to synthesize composite photocatalysts, *Chem. Rev.* 115 (2015) 10307–10377.

[38] J.T. Robinson, S.M. Tabakman, Y.Y. Liang, H.L. Wang, H.S. Casalongue, D. Vinh, H.J. Dai, Ultrasmall reduced graphene oxide with high near-infrared absorbance for photothermal therapy, *J. Am. Chem. Soc.* 133 (2011) 6825–6831.

[39] M. Li, X.J. Yang, J.S. Ren, K.G. Qu, X.G. Qu, Using graphene oxide high near-infrared absorbance for photothermal treatment of Alzheimer's disease, *Adv. Mater.* 24 (2012) 1722–1728.

[40] Z.X. Gan, X.L. Wu, M. Meng, X.B. Zhu, L. Yang, P.K. Chu, Photothermal contribution to enhanced photocatalytic performance of graphene-based nanocomposites, *ACS Nano* 8 (2014) 9304–9310.

[41] Y.H. Zhang, Z.R. Tang, X. Fu, Y.J. Xu, Engineering the unique 2D mat of graphene to achieve graphene-TiO<sub>2</sub> nanocomposite for photocatalytic selective transformation: what advantage does graphene have over its forebear carbon nanotube? *ACS Nano* 5 (2011) 7426–7435.

[42] Y.H. Zhang, Z.R. Tang, X.Z. Fu, Y.J. Xu, TiO<sub>2</sub>-graphene nanocomposites for gas-phase photocatalytic degradation of volatile aromatic pollutant: is TiO<sub>2</sub>-graphene truly different from other TiO<sub>2</sub>-carbon composite materials? *ACS Nano* 4 (2010) 7303–7314.

[43] X.M. Chen, B.Y. Su, G.H. Wu, C.J. Yang, Z.X. Zhuang, X.R. Wang, X. Chen, Platinum nanoflowers supported on graphene oxide nanosheets: their green synthesis, growth mechanism, and advanced electrocatalytic properties for methanol oxidation, *J. Mater. Chem.* 22 (2012) 11284–11289.

[44] H. Huang, D.Y.C. Leung, Complete elimination of indoor formaldehyde over supported pt catalysts with extremely low Pt content at ambient temperature, *J. Catal.* 280 (2011) 60–67.

[45] P.F. Wang, S.H. Zhan, Y.G. Xia, S.L. Ma, Q.X. Zhou, Y. Li, The fundamental role and mechanism of reduced graphene oxide in rGO/Pt-TiO<sub>2</sub> nanocomposite for high-performance photocatalytic water splitting, *Appl. Catal. B-Environ.* 207 (2017) 335–346.

[46] V. Lee, L. Whittaker, C. Jaye, K.M. Baroudi, D.A. Fischer, S. Banerjee, Large-area chemically modified graphene films: electrophoretic deposition and characterization by soft X-ray absorption spectroscopy, *Chem. Mater.* 21 (2009) 3905–3916.

[47] J.-J. Li, B. Weng, S.-C. Cai, J. Chen, H.-P. Jia, Y.-J. Xu, Efficient promotion of charge transfer and separation in hydrogenated TiO<sub>2</sub>/WO<sub>3</sub> with rich surface-oxygen-vacancies for photodecomposition of gaseous toluene, *J. Hazard. Mater.* 342 (2018) 661–669.

[48] T.M.G. Mohiuddin, A. Lombardo, R.R. Nair, A. Bonetti, G. Savini, R. Jalil, N. Bonini, D.M. Basko, C. Galiotis, N. Marzari, K.S. Novoselov, A.K. Geim, A.C. Ferrari, Uniaxial strain in graphene by Raman spectroscopy: G peak splitting, Gruneisen parameters, and sample orientation, *Phys. Rev. B* 79 (2009) 205433–205440.

[49] B. Weng, Q. Quan, Y.J. Xu, Decorating geometry- and size-controlled sub-20 nm pd nanocubes onto 2D TiO<sub>2</sub> nanosheets for simultaneous H<sub>2</sub> evolution and 1,1-dioctoxyethane production, *J. Mater. Chem. A* 4 (2016) 18366–18377.

[50] Y.H. Sang, Z.H. Zhao, J. Tian, P. Hao, H.D. Jiang, H. Liu, J.P. Claverie, Enhanced photocatalytic property of reduced graphene oxide/TiO<sub>2</sub> nanobelt surface heterostructures constructed by an *in situ* photochemical reduction method, *Small* 10 (2014) 3775–3782.

[51] M.Q. Yang, C. Han, Y.-J. Xu, Insight into the effect of highly dispersed MoS<sub>2</sub> versus layer-structured MoS<sub>2</sub> on the photocorrosion and photoactivity of CdS in graphene-CdS-MoS<sub>2</sub> composites, *J. Phys. Chem. C* 119 (2015) 27234–27246.

[52] Y. Zhang, N. Zhang, Z.-R. Tang, Y.-J. Xu, Graphene oxide as a surfactant and support for *in-situ* synthesis of Au-Pd nanoalloys with improved visible light photocatalytic activity, *J. Phys. Chem. C* 118 (2014) 5299–5308.

[53] A. Ramadoss, S.J. Kim, Improved activity of a graphene-TiO<sub>2</sub> hybrid electrode in an electrochemical supercapacitor, *Carbon* 63 (2013) 434–445.

[54] D. He, Y. Jiang, H. Lv, M. Pan, S. Mu, Nitrogen-doped reduced graphene oxide supports for noble metal catalysts with greatly enhanced activity and stability, *Appl. Catal. B-Environ.* 132 (2013) 379–388.

[55] L.L. Tan, W.J. Ong, S.P. Chai, A.R. Mohamed, Noble metal modified reduced graphene oxide/TiO<sub>2</sub> ternary nanostructures for efficient visible-light-driven photoreduction of carbon dioxide into methane, *Appl. Catal. B-Environ.* 166 (2015) 251–259.

[56] F.R. Tan, N. Wang, D.Y. Lei, W.X. Yu, X.M. Zhang, Plasmonic black absorbers for enhanced photocurrent of visible-light photocatalysis, *Adv. Optical Mater.* 5 (2017) 1–8.

[57] J.E. Lee, S. Bera, Y.S. Choi, W.I. Lee, Size-dependent plasmonic effects of M and M@SiO<sub>2</sub> (M = Au or ag) deposited on TiO<sub>2</sub> in photocatalytic oxidation reactions, *Appl. Catal. B-Environ.* 214 (2017) 15–22.

[58] A. Wood, M. Giersig, P. Mulvaney, Fermi level equilibration in quantum dot-metal nanojunctions, *J. Phys. Chem. B* 105 (2001) 8810–8815.

[59] H. Li, X.L. Cui, A hydrothermal route for constructing reduced graphene oxide/TiO<sub>2</sub> nanocomposites: enhanced photocatalytic activity for hydrogen evolution, *Int. J. Hydrogen Energ.* 39 (2014) 19877–19886.

[60] J.F. Huang, C.X. Liu, Y.H. Zhu, S. Masala, E. Alarousu, Y. Han, A. Fratalochi, Harnessing structural darkness in the visible and infrared wavelengths for a new source of light, *Nat. Nanotechnol.* 11 (2016) 60–67.

[61] L. Huang, X. Hu, S. Yuan, H. Li, T. Yan, L. Shi, D. Zhang, Photocatalytic preparation of nanostructured MnO<sub>2</sub>(Co<sub>3</sub>O<sub>4</sub>)/TiO<sub>2</sub> hybrids: the formation mechanism and catalytic application in SCR deNO<sub>x</sub> reaction, *Appl. Catal. B-Environ.* 203 (2017) 778–788.

[62] K. Zha, S. Cai, H. Hu, H. Li, T. Yan, L. Shi, D. Zhang, *In situ* DRIFTS investigation of promotional effects of tungsten on MnO<sub>x</sub>-CeO<sub>2</sub>/meso-TiO<sub>2</sub> catalysts for NO<sub>x</sub> reduction, *J. Phys. Chem. C* 121 (2017) 25243–25254.

[63] B. Weng, Y.-J. Xu, What if the electrical conductivity of graphene is significantly deteriorated for the graphene-semiconductor composite-based photocatalysis? *ACS Appl. Mater. Interface* 7 (2015) 27948–27958.

[64] S.L. Lee, J. Scott, K. Chiang, R. Amal, Nanosized metal deposits on titanium dioxide for augmenting gas-phase toluene photooxidation, *J. Nanopart. Res.* 11 (2009) 209–219.

[65] S. Weon, J. Kim, W. Choi, Dual-components modified TiO<sub>2</sub> with Pt and fluoride as deactivation-resistant photocatalyst for the degradation of volatile organic compound, *Appl. Catal. B-Environ.* 220 (2018) 1–8.

[66] P. Shen, Y.J. Liu, X.W. Huang, B. Zhao, N. Xiang, J.J. Fei, L.M. Liu, X.Y. Wang, H. Huang, S.T. Tan, Efficient triphenylamine dyes for solar cells: effects of alkyl-substituents and pi-conjugated thiophene unit, *Dyes Pigm.* 83 (2009) 187–197.

[67] N. Zhang, M.Q. Yang, S. Liu, Y. Sun, Y.J. Xu, Waltzing with the versatile platform of graphene to synthesize composite photocatalysts, *Chem. Rev.* 115 (2015) 10307–10377.

[68] Z.B. Rui, M.N. Tang, W.K. Ji, J.J. Ding, H.B. Ji, Insight into the enhanced performance of TiO<sub>2</sub> nanotube supported Pt catalyst for toluene oxidation, *Catal. Today* 297 (2017) 159–166.

[69] D.Q. Gong, H.D. Liu, G. Luo, P. Zhang, X.D. Cheng, B. Yang, Y.B. Wang, J. Min, W.X. Wang, S.P. Chen, Z.Q. Cui, K.W. Li, L.F. Hu, Thermal aging test of AlCrNO-based solar selective absorbing coatings prepared by cathodic arc plating, *Solar Energy Mater. Solar C* 136 (2015) 167–171.

[70] M. Gao, P.K.N. Connor, G.W. Ho, Plasmonic photothermal directed broadband sunlight harnessing for seawater catalysis and desalination, *Energy Environ. Sci.* 9 (2016) 3151–3160.

[71] M. Hashemi, M. Omidi, B. Muralidharan, H. Smyth, M.K. Mohagheghi, J. Mohammad, T.E. Milner, Evaluation of the photothermal properties of a reduced graphene oxide/arginine nanostructure for near-infrared absorption, *ACS Appl. Mater. Interface* 9 (2017) 32607–32620.

[72] J.-J. Li, S.-C. Cai, Z. Xu, X. Chen, J. Chen, H.-P. Jia, J. Chen, Solvothermal syntheses of Bi and Zn co-doped TiO<sub>2</sub> with enhanced electron-hole separation and efficient photodegradation of gaseous toluene under visible-light, *J. Hazard. Mater.* 325 (2017) 261–270.

[73] K.Q. Lu, N. Zhang, C. Han, F.Y. Li, Z.F. Chen, Y.J. Xu, Insight into the origin of boosted photosensitive efficiency of graphene from the cooperative experiment and theory study, *J. Phys. Chem. C* 120 (2016) 27091–27103.

[74] N. Zhang, C. Han, Y.-J. Xu, J.J. Foley, D. Zhang, J. Codrington, S.K. Gray, Y. Sun, Near-field dielectric scattering promotes optical absorption by platinum nanoparticles, *Nat. Photon.* 10 (2016) 473–482.

[75] A.A. Balandin, Thermal properties of graphene and nanostructured carbon materials, *Nat. Mater.* 10 (2011) 569–581.

[76] Y.W. Zhu, S. Murali, W.W. Cai, X.S. Li, J.W. Suk, J.R. Potts, R.S. Ruoff, Graphene and graphene oxide: synthesis, properties, and applications, *Adv. Mater.* 22 (2010) 5226–5226.

[77] E. Pop, V. Varshney, A.K. Roy, Thermal properties of graphene: fundamentals and applications, *MRS Bull.* 37 (2012) 1273–1281.

[78] M. Jablan, M. Soljacic, H. Buljan, Plasmons in graphene: fundamental properties and potential applications, *P IEEE* 101 (2013) 1689–1704.

[79] A.A. Balandin, S. Ghosh, W.Z. Bao, I. Calizo, D. Teweldebrhan, F. Miao, C.N. Lau, Superior thermal conductivity of single-layer graphene, *Nano Lett.* 8 (2008) 902–907.

[80] J.T. Hou, Y.Z. Li, M.Y. Mao, Y.Z. Yue, G.N. Greaves, X.J. Zhao, Full solar spectrum light driven thermocatalysis with extremely high efficiency on nanostructured Ce ion substituted OMS-2 catalyst for VOCs purification, *Nanoscale* 7 (2015) 2633–2640.

[81] M.Y. Mao, Y.Z. Li, J.T. Hou, M. Zeng, X.J. Zhao, Extremely efficient full solar spectrum light driven thermocatalytic activity for the oxidation of VOCs on OMS-2 nanorod catalyst, *Appl. Catal. B-Environ.* 174 (2015) 496–503.

[82] N.Y. Tetsuro Selyama, Kolchi Eguchi, Characterization and activity of some mixed metal oxide catalysts, *Ind. Eng. Chem. Prod. Res. Dev.* 24 (1985) 19–27.

[83] Y. Zheng, W. Wang, D. Jiang, L. Zhang, X. Li, Z. Wang, Ultrathin mesoporous Co<sub>3</sub>O<sub>4</sub> nanosheets with excellent photo-/thermo-catalytic activity, *J. Mater. Chem. A* 4 (2016) 105–112.

[84] C. Deng, B. Li, L. Dong, F. Zhang, M. Fan, G. Jin, J. Gao, L. Gao, F. Zhang, X. Zhou, NO reduction by CO over CuO supported on CeO<sub>2</sub>-doped TiO<sub>2</sub>: the effect of the amount of few CeO<sub>2</sub>, *Phys. Chem. Chem. Phys.* 17 (2015) 16092–16109.

[85] M.R. Morales, M. Pilar Yeste, H. Vidal, J.M. Gatica, L.E. Cadus, Insights on the combustion mechanism of ethanol and n-hexane in honeycomb monolithic type catalysts: influence of the amount and nature of Mn-Cu mixed oxide, *Fuel* 208 (2017) 637–646.

[86] A.R. Puigdollers, P. Schlexer, S. Tosoni, G. Pacchioni, Increasing oxide reducibility: the role of metal/oxide interfaces in the formation of oxygen vacancies, *ACS Catal.* 7 (2017) 6493–6513.

[87] Y. Li, J. Huang, T. Peng, J. Xu, X. Zhao, Photothermocatalytic synergistic effect leads to high efficient detoxification of benzene on TiO<sub>2</sub> and Pt/TiO<sub>2</sub> nanocomposite, *ChemCatChem* 2 (2010) 1082–1087.

[88] S. Swislocki, K. Stoebe, W.F. Maier, Catalysts for selective propane oxidation in the presence of carbon monoxide: mechanistic aspects, *J. Catal.* 316 (2014) 219–230.

[89] Y.G. Wang, D.C. Cantu, M.S. Lee, J. Li, V.A. Glezakou, R. Rousseau, CO oxidation on Au/TiO<sub>2</sub>: condition-dependent active sites and mechanistic pathways, *J. Am. Chem. Soc.* 138 (2016) 10467–10476.

[90] M.J. Wang, F. Zhang, X.D. Zhu, Z.M. Qi, B. Hong, J.J. Ding, J. Bao, S. Sun, C. Gao, DRIFTS evidence for facet-dependent adsorption of gaseous toluene on TiO<sub>2</sub> with relative photocatalytic properties, *Langmuir* 31 (2015) 1730–1736.

[91] X. Wang, H. Shi, J.H. Kwak, J. Szanyi, Mechanism of CO<sub>2</sub> hydrogenation on Pd/Al<sub>2</sub>O<sub>3</sub> catalysts: kinetics and transient DRIFTS-MS studies, *ACS Catal.* 5 (2015) 6337–6349.

[92] W.C. Wilfong, C.S. Srikanth, S.S.C. Chuang, *In situ* ATR and DRIFTS studies of the nature of adsorbed CO<sub>2</sub> on tetraethylenepentamine films, *ACS Appl. Mater. Interface* 6 (2014) 13617–13626.

[93] H. Sun, Z.G. Liu, S. Chen, X. Quan, The role of lattice oxygen on the activity and selectivity of the OMS-2 catalyst for the total oxidation of toluene, *Chem. Eng. J.* 270 (2015) 58–65.

[94] D. Widmann, R.J. Behm, Activation of molecular oxygen and the nature of the active oxygen species for CO oxidation on oxide supported Au catalysts, *Acc. Chem. Res.* 47 (2014) 740–749.